Supporting Information

Iron Carbide Nanoparticles Supported on N-Doped Carbon Porous Framework as Bifunctional Material for Electrocatalytic Oxygen Reduction and Supercapacitor

Zengyu Han[a], Wenfang Cai[b], Shifeng Zhao[c], Yi Zhao[c], Jirui Bai[a], Qingyun Chen[c], Yunhai Wang[a,*]

[a] *Department of Environmental Science and Engineering, School of Energy and Power Engineering, Xi'an Jiaotong University, Xi'an 710049, China*

[b] *School of Chemical Engineering and Technology, Xi'an Jiaotong University, Xi'an 710049, China*

[c] *International Research Center for Renewable Energy (IRCRE), State Key Laboratory of Multiphase Flow in Power Engineering (MFPE), Xi'an Jiaotong University, Xi'an 710049, China*

* Corresponding author at: Xi'an Jiaotong University, Xi'an, Shaanxi 710049, PR China. Tel.: +86 29 82668572. E-mail address: wang.yunhai@mail.xjtu.edu.cn

1. Experimental section

1.1. Synthesis of catalysts

Firstly, urea (0.12 g), glucose (0.5 g), iron (III) nitrate nonahydrate ($Fe(NO_3)_3 \cdot 9H_2O$) (0.8 mmol), sodium chloride (NaCl) (0.75 g) were mixed together and dissolved in ultrapure water (5 mL) to form homogeneous solutions. Secondly, the mixture was transferred into a crucible and heated at 80 °C for 24 h to remove water and cooled down naturally to room temperature. The above dried precursor and urea were placed in a tube furnace under Ar flow with urea upstream and heated with a rate of 5 °C min^{-1} to 750 °C and kept for 2 h in Ar atmosphere. Then the annealing products were leached in 4 M HCl solution at 80 °C for 2 h, followed by centrifugation and thoroughly washing with deionized water. The resulting black precipitate was dried in a vacuum oven for further use, referred to as Fe_3C/PNCF. For comparison, the Fe_3C-based N-doped carbon (denoted as Fe_3C/NC) and Fe_3C-based porous carbon (Fe_3C/PNC) materials were prepared by the same procedure as Fe_3C/PNCF, except the raw materials without the addition of NaCl and urea upstream nitrogenization, respectively.

1.2. Physicochemical characterization

XRD patterns were collected by X-ray diffractometer (PANalytical, Cu Kα, λ = 0.15406 nm, 40 kV, 40 mA,). Field emission scanning electron microscope (FE-SEM, JEOL JSM-7800F) with energy-dispersive X-ray detector (OXFORD MAX-80), and transmission electron microscopy (TEM, G2F30 FEI) were used for morphology and structure characterization as well as elemental analysis. Raman spectra were collected on HORIBA JOBIN YVON HR800 spectrometer system equipped with a 532 nm laser excitation source. The specific surface areas (SSAs) determined by the Brunauer-Emmett-Teller (BET) equation and pore volume calculated based on the BJH (Barrett–Joyner–Halenda) model of synthesized samples were carried out on a Micromeritics ASAP 2020.

The XPS spectrum was collected using an AXIS UL TRABLD equipped with an Al Ka (1486.6 eV) excitation source, referenced to C 1s binding energy (BE) of 284.8 eV. The

valence bands recorded with monochromatized Al Kα radiation are most closely comparable to the ground state density of states (DOS), as the XPS-derived energy scale can be used to correct the DOS calculations and further draw conclusions about the true ground-state d-band structure[1, 2].

The position of the d-band center (ε_d) from the valence band spectrum (VBS) is given by equation (1):

$$\varepsilon_d = \int R(\varepsilon)\varepsilon d\varepsilon / \int R(\varepsilon) d\varepsilon \qquad (1)$$

where the $R(\varepsilon)$ is the XPS intensity from the measured spectra after Shirley background subtraction[3]. The background subtracted spectra were integrated up to 8.75 eV BE with respect to Fermi level for accurate comparison[4].

The contact angles of as-prepared samples were measured using the sessile drop technique by a contact angle meter (SL200B, Shanghai Zhongchen Digital Technology Apparatus Co. Ltd, China). 3 μL water droplet was dropped onto a pressed and leveled sample layer, and the images of the water droplet were captured by a camera.

1.3. Electrochemical measurements

1.3.1. Electrocatalytic activity for ORR

The electrochemical measurements for ORR were carried out in a three-electrode cell by using an electrochemical workstation (CHI 760E), with a reference electrode (Hg/HgO, 0.1 M KOH), a counter electrode (graphite rod, Φ = 0.5 cm), and 0.1 M KOH aqueous solution saturated with O_2 or N_2 as the electrolyte. The catalyst (2 mg) was dispersed with ethanol (495 μL), ultrapure water (495 μL), and Nafion® (5 wt%, 10 μL), with ultrasonication for 30 min. The formed ink was dropped on a polished glassy carbon electrode (GCE, Φ = 4 mm) with a mass loading of 0.28 mg cm^{-2}, and dried at room temperature, serving as the working electrode. Prior to the test, a cyclic voltammetry (CV) measurement with at least 10 cycles was conducted for activating the catalyst. For comparison, commercial Pt/C (20wt%) modified GCE was prepared and tested similarly.

Rotating disk electrode (RDE) measurements: For RDE measurements, catalysts were

scanned from 1.2 V to 0.3 V vs. RHE at a scan rate of 10 mV s^{-1} with varying rotation speeds from 400 rpm to 2025 rpm. Koutecky–Levich plots were derived from RDE measurements to calculate the critical kinetic parameters based on the following Koutecky-Levich equation (2) to (5):

$$\frac{1}{j}=\frac{1}{j_d}+\frac{1}{j_K}=\frac{1}{B\omega^{1/2}}+\frac{1}{j_K} \quad (2)$$

$$B=0.62nFC_0D_0^{\frac{2}{3}}\nu^{-\frac{1}{6}} \quad (3)$$

$$j_d=B\omega^{1/2} \quad (4)$$

$$J_k=\frac{J\times J_L}{J_L-J} \quad (5)$$

where j is the measured current density, jk and jd are the kinetic- and diffusion-limiting current densities, ω is the angular velocity, n is transferred electrons number, F is the Faraday constant (96485 C mol^{-1}), C_0 is the bulk concentration of O_2 (1.26×10^{-6} mol cm^{-3}), D_0 is the diffusion coefficient of O_2 in electrolyte (1.9×10^{-5} cm^2 s^{-1}) and v is the kinematic viscosity (0.01 cm^2 s^{-1}) of 0.1 M KOH.

All LSV curves were corrected with background currents collected in N_2-saturated 0.1 M KOH. All potentials in the RDE test were converted to potentials vs. RHE by $E_{RHE} = E_{Hg/HgO} + 0.8663$ V, based on the calibration results, and corrected with 90% iR-compensation. The onset potential is defined at cathodic current of 0.1 mA cm^{-2}.

The electrochemical active surface area (ECSA) of the catalysts was estimated by dividing the double-layer capacitances (C_{dl}) by the specific capacitance (general as $C_{s(cat)}$ of 40 μF·cm^{-2} in 0.1M KOH) as shown in equation (6)[5, 6]. The double layer capacitance was measured via CV tests at different scan rates of 10, 20, 40, 60, 80, and 100 mV s^{-1} in the non-Faradaic process region from 0.15 V to 0.25 V (vs. Hg/HgO) for ORR in N_2-saturated electrolyte, as equation (7).

$$ECSA=\frac{C_{dl}}{C_{s(cat)}} \quad (6)$$

$$C_{dl}=\frac{(J_a-J_c)/2}{\nu} \quad (7)$$

where C_{dl} is the double-layer capacitance, J_a and J_c are the positive and negative scan currents at 0.2 V (vs. Hg/HgO), respectively, and ν is the scan rate.

The electrochemical impedance spectroscopy (EIS) was taken at 0V (vs Hg/HgO) (0.866 V vs. RHE) in the frequency range of 0.01 Hz–100 kHz with an amplitude of 5 mV. Methanol tolerance tests were performed by chronoamperometry at 0.37 V vs. RHE (-0.5 V vs. Hg/HgO), by adding 15 vol% of methanol at 200 s.）

Rotating ring-disk electrode (RRDE) measurements were recorded to determine the selectivity of the four-electrons reactions. The RRDE consisted of a glassy carbon disk (0.12566 cm^2) and Pt ring (4.3 mm ring inner diameter, 6.2 mm outer diameter). And RRDE measurements were conducted by linear sweep voltammetry (LSV) from 0.36 V to -0.6 V vs. Hg/HgO (1.23 V to 0.27 V vs. RHE) at a scan rate of 10 mV s^{-1} at 1600 rpm, while the ring electrode was held at 1.2 V vs. RHE.

The electrons transfer number (n)and the hydrogen peroxide yield (H_2O_2 %) were calculated from the ring current (I_r) and the disk current (I_d), according to equations (8) and (9), respectively:

$$n = \frac{4I_d}{N^{-1}I_r + I_d} \qquad (8)$$

$$H_2O_2\% = 200\frac{I_r}{I_r + NI_d} = 200\frac{N^{-1}I_r}{N^{-1}I_r + I_d} \qquad (9)$$

where I_d stands for the Faradaic current at the disk, I_r is the Faradaic current at the ring, and N is the H_2O_2 collection coefficient at the ring (N = 0.47), which is mainly related to the size of the disk or ring of the working electrode.

1.3.2. Supercapacitive performance

Electrochemical measurements for the supercapacitor were performed on an electrochemical workstation (CHI 760E, CH Instrument) using a conventional three-electrode cell, and the auxiliary and reference electrodes were Pt sheet and Hg/HgO, respectively. The electrolyte was 6 M KOH aqueous solution. The working electrode was prepared as follows: 80 wt % active material (24 mg), 10 wt % acetylene black (3 mg), and 10 wt % poly(tetrafluoroethylene) (PTFE, 3 mg) were dispersed in 1.5 mL of ethanol. Thereinto, acetylene black, and PTFE were used as the conductive agent and binder, respectively. Then 90 μL of the above as-prepared solution was dropped on a

nickel foam (1.0 cm^2) and dried at vacuum. This composite Ni foam electrode was pressed at 1.0 MPa for 1 min before the electrochemical experiment. Cyclic voltammetry (CV) curves were obtained in a potential range from -1 to 0 V vs. Hg/HgO at various scanning rates of 10, 20, 50, and 100 mV s^{-1}, respectively. Galvanostatic charge/discharge (GCD) measurements were calculated from -1 to 0 V with different current densities (1, 2, 4, 8, 10, 16, 20 and 32 A g^{-1}). According to the GCD results, the gravimetric specific capacitance C_s (F g^{-1}) was calculated according to the equation (10):

$$C_s = \frac{I \times \Delta t}{m \times \Delta V} \qquad (10)$$

where I is the constant current applied to the measurement, m is the mass of active material on Ni foam, ΔV is the discharge potential range, and Δt is the discharge time.

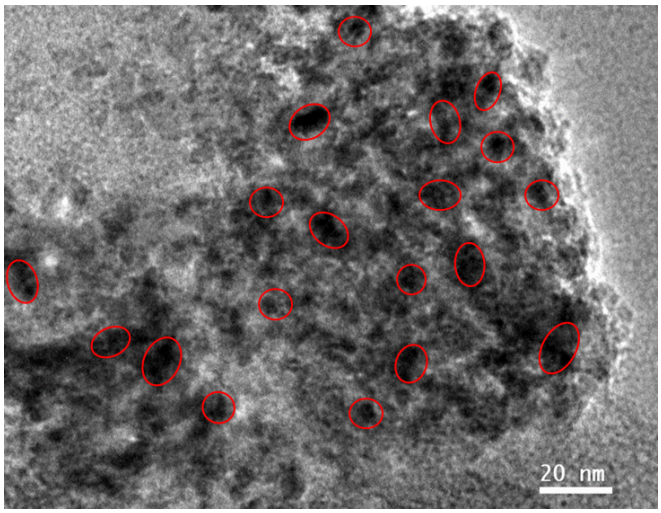

Fig. S1 TEM image of Fe_3C NPs decorated porous N-doped carbon framework (Fe_3C/PNCF). The red circles highlight some Fe_3C nanoparticles, embedded on the N-doped carbon framework.

Table S1 Nitrogen sorption data for the as-prepared samples.

Catalysts	SA[a] [m^2g^{-1}]	PV[b] [cm^3g^{-1}]
[Fe_3C/PNCF]	711.6	0.48
[Fe_3C/NC]	250.1	0.16
[Fe_3C/PNC]	899.1	2.47

[a] BET surface area; [b] Pore volume determined by the BJH method.

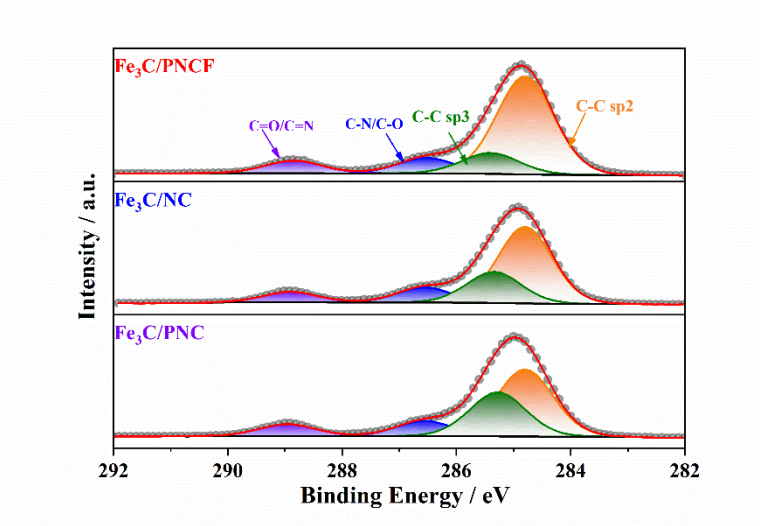

Fig. S2 XPS high-resolution C 1s spectra for the synthesized samples.

Table S2 Chemical composition and element content of the synthesized samples detected by XPS.

Catalyst	C(at%)	N(at%)	O(at%)	Fe(at%)
	(atom %)			
[Fe_3C/PNCF]	86.25	2.43	11.10	0.22
[Fe_3C/NC]	86.09	0.17	13.61	0.13
[Fe_3C/PNC]	86.56	0.07	13.32	0.05

Table S3 Deconvolution results of C 1s XPS spectra of the synthesized samples.

Catalyst	C-C sp2	C-C sp3	C-N/C-O	C=O/C=N
	(rel. %)			
[Fe_3C/PNCF]	66.67	14.24	10.57	8.52
[Fe_3C/NC]	57.45	23.31	11.32	7.93
[Fe_3C/PNC]	48.56	31.86	10.98	8.60

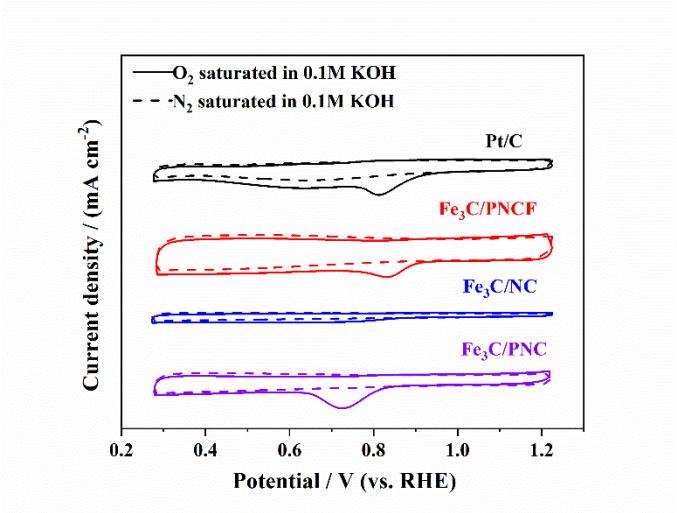

Fig. S3 ORR CV curves of commercial Pt/C, and as-prepared samples in N_2 or O_2 saturated 0.1 M KOH.

Table S4 ORR performance of commercial Pt/C, and the as-prepared samples. (including onset potential, half-wave potential, electron transfer number, selective productivity of H_2O_2, electrochemically active surface area (ECSA).)

Catalyst	E_{Onset} [V vs. RHE]	$E_{1/2}$ [V vs. RHE]	n	H_2O_2%	S_{ECSA} [cm^2]
[Fe_3C/PNCF]	0.95	0.84	3.9	4.1	55.75
[Fe_3C/NC]	0.88	0.69	3.5	25.2	12.75
[Fe_3C/PNC]	0.88	0.79	3.6	20.5	28.50
Pt/C	0.94	0.83	4.0	0.6	18.00

Table S5 Values of the equivalent circuit elements based on the EIS analysis of as-prepared samples.

Sample	R_s [Ω cm^2]	R_{ct} [Ω cm^2]
[Fe_3C/PNCF]	6.65	26.20
[Fe_3C/NC]	7.78	259.36
[Fe_3C/PNC]	7.18	130.06
[Pt/C]	6.45	41.35

The fitting results corresponding to equivalent circle diagrams of R(C(R)) derived from the electrochemical fitting software (Zview), which could match the experimental data well. R_s and R_{ct} from the equivalent circle could be attributed to the solution resistance and charge transfer resistance, respectively.

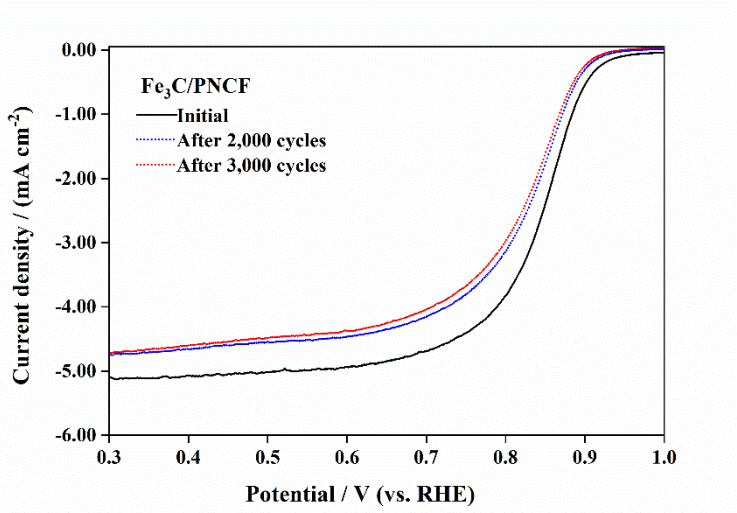

Fig. S4 LSV curve of Fe_3C/PNCF before, and after 2000 and 3000 CV cycles.

Table S6 Comparison of ORR performance between Fe_3C/PNCF in this work and several representative electrocatalyst with high performance in 0.1M KOH.

Catalysts	Loading (mg cm^{-2})	E_{onset} (V *vs.* RHE)	$E_{1/2}$ (V *vs.* RHE)	J_d (mA cm^{-2})	References
Fe_3C/PNCF	0.28	0.95	0.84	5.64	This work
FeCo@N-HC	0.42	0.98	0.85	/	[7]
$(Fe_2N/MNGCS)_4$	0.40	0.96	0.881	7.18	[8]
Fe-CZIF-800-10	0.22	0.982	0.83	5.68	[9]
MZ8-S-P	0.4	0.964	0.855	5.89	[10]
$NHPC_{1:3}$-900	0.42	/	0.87	5.7	[11]
OHEA-mNC	0.40	/	0.9	5.7	[12]
Fe/Meso-NC-100	0.34	0.97	0.885	6.4	[13]
Fe-N/P-C-700	0.60	0.941	0.867	5.66	[14]
Co-SAC@NC	0.612	0.96	0.82	4.96	[15]
Fe/N/S-PCNT	0.1	0.96	0.84	/	[16]
Fe/Fe_3C@NdC-NCs	0.2	/	0.83	5.82	[17]
Fe_3C@NP-PCF	0.46	0.9037	0.8015	5.68	[18]
FeCo-NSC	0.4	0.93	0.86	5.26	[19]
Fe–N–C/MXene	0.1	0.92	0.84	/	[20]
Fe SA-NSC-900	0.1	0.94	0.86	/	[21]
FeBNC-800	0.6	0.968	0.838	5.51	[22]

Note: FeCo@N-HC (N-doped honeycombed carbon); $(Fe_2N/MNGCS)_4$ (ultra-small Fe_2N nanocrystals were incorporated into mesoporous nitrogen-doped graphitic carbon spheres); Fe-CZIF-800-10 (N-doped hierarchical porous carbons); MZ8-S-P (NaCl/ZIF-8 derived interconnected carbon networks); $NHPC_{1:3}$-900 (N-doped hierarchical porous carbons derived from NaCl and ZIF-8); OHEA-mNC (ordered high-entropy alloys-mesoporous nitrogen-rich carbon sandwich framework); Fe/Meso-NC-100 (Meso-NC-supported Fe SAC secondary heat-treated at 1000 ℃); Fe-N/P-C-700 (carbon nanosheets embedded with nitrogen and phosphorus dual-coordinated iron active sites); Fe/N/S-PCNT (Fe/N/S-doped porous carbon nanotube); Fe/Fe_3C@NdC-NCs (core–shell-structured Fe/Fe_3C@N-doped-carbon nanorod-clusters); Fe-N/P-C-700 (carbon nanosheets with nitrogen and phosphorus dual-coordinated iron active sites); Fe_3C@NP-PCF (Fe_3C-embedded N and P-co-doped porous carbon hybrid nanowires); FeCo-NSC (coordination with N and S heteroatoms); Fe SA-NSC-900 (atomically dispersed Fe–heteroatom (N, S) bridge sites anchored on carbon nanosheets); FeBNC-800 (B-decorated porous carbon frameworks with atomically dispersed Fe–Nx species).

Table S7 Comparison of supercapacitor performance of Fe_3C/PNCF with other carbon-based materials in 6M KOH.

Material	Gravimetric capacitance (F g^{-1})	Current density (A g^{-1})	References
Fe_3C/PNCF	385.3	1	This work
	320	20	
Fe-CZIF-800-10	214	1	[9]
N-doped foam-like carbon plate	338	1	[23]
	200	20	
LC-co3DOm carbons	284	1	[24]
PCS-0.88	338	1	[25]
GPCN-SS-800	294	1	[26]
PCNS/RHC_8	315	0.1	[27]
HMC-800	340	1	[28]
KPAC-800	306	1	[29]
N,S-PCNs1-1	298	0.5	[30]
tubular g-C_3N_4	233	0.2	[31]
	204	0.5	

Note: Fe-CZIF-800-10 (ZIF-derived carbon with Fe/Fe_3C); LC-co3DOm carbons (Co-assembled 3D Ordered Mesoporous with low incipient glucose concentrations); PCS-0.88 (pomegranate-like carbon microsphere); GPCN-SS-800 (Graphene-like porous carbon nanosheets- Salvia splendens); PCNS/RHC_8 (porous carbon nanosheets/rice husk-derived carbon); HMC-800 (micro/mesoporous carbon); KPAC-800 (hierarchically porous activated carbons); N,S-PCNs1-1 (nitrogen and sulfur co-doped porous carbon nanosheets).

References

1. T. Hofmann, T. H. Yu, M. Folse, L. Weinhardt, M. Bar, Y. F. Zhang, B. V. Merinov, D. J. Myers, W. A. Goddard and C. Heske, *Journal of Physical Chemistry C*, 2012, **116**, 24016-24026.
2. X. Q. Wu, F. Y. Chen, N. Zhang, Y. M. Lei, Y. C. Jin, A. Qaseem and R. L. Johnston, *Small*, 2017, **13**, 1603387.
3. V. R. Stamenkovic, B. Fowler, B. S. Mun, G. Wang, P. N. Ross, C. A. Lucas and N. M. Markovic, *Science*, 2007, **315**, 493-497.
4. V. R. Stamenkovic, B. S. Mun, M. Arenz, K. J. J. Mayrhofer, C. A. Lucas, G. Wang, P. N. Ross and N. M. Markovic, *Nature Materials*, 2007, **6**, 241-247.
5. S. R. Choi, J.-I. Lee, H. Park, S. W. Lee, D. Y. Kim, W. Y. An, J. H. Kim, J. Kim, H.-S. Cho and J.-Y. Park, *Chemical Engineering Journal*, 2021, **409**, 128226.
6. C. C. L. McCrory, S. Jung, J. C. Peters and T. F. Jaramillo, *Journal of the American Chemical Society*, 2013, **135**, 16977-16987.
7. Z. Han, S.-Y. Lin, J.-J. Feng, L. Zhang, Q.-L. Zhang and A.-J. Wang, *International Journal of Hydrogen Energy*, 2021, **46**, 19385-19396.
8. J. Xiao, Y. Xu, Y. Xia, J. Xi and S. Wang, *Nano Energy*, 2016, **24**, 121-129.
9. G. Li, J. Zhang, W. Li, K. Fan and C. Xu, *Nanoscale*, 2018, **10**, 9252-9260.
10. Y. Qian, T. An, K. E. Birgersson, Z. Liu and D. Zhao, *Small*, 2018, **14**, 1704169.
11. C. Xuan, B. Hou, W. Xia, Z. Peng, T. Shen, H. L. Xin, G. Zhang and D. Wang, *Journal of Materials Chemistry A*, 2018, **6**, 10731-10739.
12. G. Zhu, Y. Jiang, H. Yang, H. Wang, Y. Fang, L. Wang, M. Xie, P. Qiu and W. Luo, *Advanced Materials*, 2022, **34**, 2110128.
13. S.-N. Zhao, J.-K. Li, R. Wang, J. Cai and S.-Q. Zang, *Advanced Materials*, 2022, **34**, 2107291.
14. K. Yuan, D. Luetzenkirchen-Hecht, L. Li, L. Shuai, Y. Li, R. Cao, M. Qiu, X. Zhuang, M. K. H. Leung, Y. Chen and U. Scherf, *Journal of the American Chemical Society*, 2020, **142**, 2404-2412.
15. X. Han, X. Ling, Y. Wang, T. Ma, C. Zhong, W. Hu and Y. Deng, *Angewandte Chemie-International Edition*, 2019, **58**, 5359-5364.
16. Z. Tan, H. Li, Q. Feng, L. Jiang, H. Pan, Z. Huang, Q. Zhou, H. Zhou, S. Ma and Y. Kuang, *Journal of Materials Chemistry A*, 2019, **7**, 1607-1615.
17. Z. Cao, H. Hu, M. Wu, K. Tang and T. Jiang, *Journal of Materials Chemistry A*, 2019, **7**, 17581-17593.
18. M. Li, Y. Liu, L. Han, J. Xiao, X. Zeng, C. Zhang, M. Xu, P. Dong and Y. Zhang, *Journal of Materials Chemistry A*, 2019, **7**, 17923-17936.
19. Y. Wu, C. Ye, L. Yu, Y. Liu, J. Huang, J. Bi, L. Xue, J. Sun, J. Yang, W. Zhang, X. Wang, P. Xiong and J. Zhu, *Energy Storage Materials*, 2022, **45**, 805-813.
20. L. Jiang, J. Duan, J. Zhu, S. Chen and M. Antonietti, *Acs Nano*, 2020, **14**, 2436-2444.
21. M. Wang, W. Yang, X. Li, Y. Xu, L. Zheng, C. Su and B. Liu, *Acs Energy Letters*, 2021, **6**, 379-386.

22. K. Yuan, S. Sfaelou, M. Qiu, D. Lutzenkirchen-Hecht, X. Zhuang, Y. Chen, C. Yuan, X. Feng and U. Scherft, *Acs Energy Letters*, 2018, **3**, 252-260.
23. Y. Dong, W. Wang, H. Quan, Z. Huang, D. Chen and L. Guo, *Chemelectrochem*, 2016, **3**, 814-821.
24. Z. Tian, M. Sharma, C. A. Wade, M. Watanabe and M. A. Snyder, *Acs Applied Materials & Interfaces*, 2019, **11**, 43509-43519.
25. S. Feng, Z. Liu, Q. Yu, Z. Zhuang, Q. Chen, S. Fu, L. Zhou and L. Mai, *Acs Applied Materials & Interfaces*, 2019, **11**, 4011-4016.
26. B. Liu, M. Yang, H. Chen, Y. Liu, D. Yang and H. Li, *Journal of Power Sources*, 2018, **397**, 1-10.
27. S. Dong, X. He, H. Zhang, X. Xie, M. Yu, C. Yu, N. Xiao and J. Qiu, *Journal of Materials Chemistry A*, 2018, **6**, 15954-15960.
28. W. Qian, F. Sun, Y. Xu, L. Qiu, C. Liu, S. Wang and F. Yan, *Energy & Environmental Science*, 2014, **7**, 379-386.
29. P. Cheng, S. Gao, P. Zang, X. Yang, Y. Bai, H. Xu, Z. Liu and Z. Lei, *Carbon*, 2015, **93**, 315-324.
30. Y. Li, G. Wang, T. Wei, Z. Fan and P. Yan, *Nano Energy*, 2016, **19**, 165-175.
31. M. Tahir, C. Cao, F. K. Butt, F. Idrees, N. Mahmood, Z. Ali, I. Aslam, M. Tanveer, M. Rizwan and T. Mahmood, *Journal of Materials Chemistry A*, 2013, **1**, 13949-13955.